Journal of the Optical Society of America A
OPTICS, IMAGE SCIENCE, AND VISION

Ultrasound-modulated optical tomography: direct recovery of elasticity distribution from experimentally measured intensity autocorrelation

K. P. Mohanan,[1] A. K. Nandakumaran,[2] D. Roy,[3] and R. M. Vasu[1,*]

[1]Department of Instrumentation and Applied Physics, Indian Institute of Science, Bangalore 560012, India
[2]Department of Mathematics, Indian Institute of Science, Bangalore 560012, India
[3]Computational Mechanics Lab, Department of Civil Engineering, Indian Institute of Science, Bangalore 560012, India
*Corresponding author: vasu@isu.iisc.ernet.in

Received 4 December 2014; revised 23 March 2015; accepted 23 March 2015; posted 24 March 2015 (Doc. ID 229022); published 29 April 2015

Based on an ultrasound-modulated optical tomography experiment, a direct, quantitative recovery of Young's modulus (E) is achieved from the modulation depth (M) in the intensity autocorrelation. The number of detector locations is limited to two in orthogonal directions, reducing the complexity of the data gathering step whilst ensuring against an impoverishment of the measurement, by employing ultrasound frequency as a parameter to vary during data collection. The M and E are related via two partial differential equations. The first one connects M to the amplitude of vibration of the scattering centers in the focal volume and the other, this amplitude to E. A (composite) sensitivity matrix is arrived at mapping the variation of M with that of E and used in a (barely regularized) Gauss–Newton algorithm to iteratively recover E. The reconstruction results showing the variation of E are presented.

OCIS codes: (170.3880) Medical and biological imaging; (170.3660) Light propagation in tissues; (170.7180) Ultrasound diagnostics; (170.6960) Tomography; (170.3010) Image reconstruction techniques; (170.4580) Optical diagnostics for medicine.

http://dx.doi.org/10.1364/JOSAA.32.000955

1. INTRODUCTION

In ultrasound-modulated optical tomography (UMOT) [1,2] a focused ultrasound (US) beam has been introduced to mark out a localized region in a biological object for imaging with coherent light. Since the US beam can be tightly focused in tissue, a remedy for poor spatial resolution in the optical contrast recovery in diffuse optical tomography can be had through UMOT. The US beam introduces a modulation of the refractive index, $n(\mathbf{r})$, and additional dynamics, over and above the temperature-induced Brownian motion, to the scattering centers in the focal region referred to as the region of interest (ROI) in the object [3,4]. Owing to these, a coherent light beam interrogating the object picks up a phase modulation from the insonified ROI, which appears as a modulation on the overall decay of the specific intensity, $I(\mathbf{r}, \hat{k}_s, \tau)$. The specific intensity $I(\mathbf{r}, \hat{k}_s, \tau)$ is derived from the mutual coherence function of light, $\langle E_a(\mathbf{r}_a, t)E_b^*(\mathbf{r}_b, t+\tau)\rangle$ expressed in center of gravity coordinates (i.e., $\mathbf{r} = (\mathbf{r}_a + \mathbf{r}_b/2)$, with $\hat{k}_s$ representing the normalized scattered light propagation vector in the direction $\mathbf{r}_b - \mathbf{r}_a$). The property of light followed here is an angle-averaged version of $I(\mathbf{r}, \hat{k}_s, \tau)$, called the amplitude autocorrelation, $G(\mathbf{r}, \tau)$. The intensity autocorrelation $g_2(\mathbf{r}, \tau)$ which is the experimental measurement, is related to $g_1(\mathbf{r}, \tau) = (G(\mathbf{r}, \tau)/G(\mathbf{r}, 0))$ and has a modulation, M, owing to the phase modulation picked up by the specific intensity of light in its passage through the ROI. From M, the optical and mechanical properties of the material in the ROI can be reconstructed. The typical mechanical property is the Young's modulus which influences the amplitude of oscillation of the scattering centers. In an earlier work [5], we demonstrated the recovery of $p(\mathbf{r})$, the distribution of the mean-squared amplitude of vibration of the scattering centers in the object undergoing nearly sinusoidal oscillation under local US forcing (i.e., $p(\mathbf{r}) = \langle|A^2(\mathbf{r})|\rangle$, where $A(\mathbf{r})$ is the amplitude of vibration and $\langle\rangle$ represents averaging over a volume $(l^*)^3$ with l^* denoting the transport-mean-free path of photons) from M. The readily measured quantity in an experiment is $g_2(\mathbf{r}, \tau)$ on the boundary of the object, from which M (the experimental measurement) can be computed (see [6] for the relation between g_1 and g_2). Since the local absorption coefficient $\mu_a(\mathbf{r})$, $p(\mathbf{r})$ and $n(\mathbf{r})$ influence M, it should be possible (at least theoretically) to recover all the above three parameters pertaining to the ROI from M. For this, a perturbation equation is

set up from the correlation diffusion equation (CDE) describing the propagation of $G(\mathbf{r}, \tau)$ in a turbid medium [5], thus connecting the US-induced perturbations in the ROI [which are in $n(\mathbf{r})$ and mechanical vibration of the scattering centers] to M, which is the perturbation of $G(\mathbf{r}, \tau)$. This equation, relating $p(\mathbf{r})$ nonlinearly to M (as in [5]), is solved either as it is, or, for ease of computation, after linearization at $p = 0$. The solution involves finding $p(\mathbf{r})$ which minimizes $\epsilon(p) = \frac{1}{2}\|M - \mathcal{M}\|^2$, where M is the experimentally measured modulation depth and $\mathcal{M}$ its computationally obtained counterpart [$\mathcal{M}$ may be looked upon as a function of $p(\mathbf{r})$]. In [5], the above minimization is achieved by employing an iterative regularized Gauss–Newton algorithm.

Even though $p(\mathbf{r})$ gives an indication of the mechanical stiffness of the object, a more appropriate parameter to recover is Young's modulus (E). With this in mind, this work demonstrates the direct recovery of E from experimentally measured M without recovering $p(\mathbf{r})$ *en route*. An additional partial differential equation (PDE) is required, the momentum balance equation connecting $A(\mathbf{r})$ to $E(\mathbf{r})$. The last equation may be viewed as a constraint that $p(\mathbf{r})$, entering the propagation equation of $G(\mathbf{r}, \tau)$, should satisfy. We note in passing that in this work we do not approach the inverse problem of recovery of $E(\mathbf{r})$ from M as a PDE-constrained optimization problem (as is done in the context of diffuse optical tomography in [7,8]); instead, we employ the two PDEs to arrive at a composition to compute $\mathcal{M}$ given $E(\mathbf{r})$ and also the required sensitivity matrices. The Jacobian matrix giving the rate of change of $\mathcal{M}$ with respect to E is obtained as a composition of the sensitivity of $\mathcal{M}$ with respect to p and p with respect to E wherein the measurement operator connecting A to p is also employed. For the recovery of E we follow the Gauss–Newton algorithm which sets up and solves a perturbation equation by locally linearizing the equation connecting $\mathcal{M}$ to E at the current estimate of E.

Apart from the direct recovery of E, a novelty of this work is the introduction of a greatly simplified data collection modality. In order to gather a sufficiently large set of orthogonal data, we do not so much increase the number of detectors, but scan the frequency of the ultrasound source, resulting in a set of measurements, M, whilst limiting the number of detectors. Since a measurement with good signal-to-noise ratio requires painstaking alignment of a single speckle to a single-mode optical fiber, for a tomography experiment using many detectors, maintenance of a multitude of detectors in proper alignment is too cumbersome to be practically realizable. This justifies the reduction of the number of detectors and the introduction of another parameter, namely, the US frequency, by the variation of which, as shown in this work, we could gather sufficient independent data to make the inverse problem computationally tractable. If $p(\mathbf{r})$ is retained as the primary unknown, along with the acoustic frequency, the dimension of the problem also increases posing a challenge to an accurate reconstruction. However, by projecting $p(\mathbf{r})$ to $E(\mathbf{r})$, the latter being invariant to the acoustic frequency, through the momentum balance equation applied to the vibrating US focal region, we escape the growth of the problem dimension and the consequent instability of the inversion algorithm. As mentioned earlier, the experimental simplification achieved, as seen in Section 4 below, is that we get enough independent data with barely one, or at most two, detectors. (The concept of varying the ultrasound frequency was introduced in an earlier work by some of us [9] in the context of UMOT. In this, the objective was to recover the elastic modulus of the insonified region, considered homogenous with a single value, from the measured natural frequency of the vibrating region obtained from the peak of the speckle modulation depth. In the present work the insonified region is inhomogenous and our objective is to recover $E(\mathbf{r})$ tomographically from a set of modulation depths measured around this peak.)

The rest of the paper is organized as follows. In Sections 2 and 3 the forward models connecting the measurement to E via the US-induced amplitude of vibration are introduced. With these as the forward models, Section 4 gives the recovery of $E(\mathbf{r})$ by solving a mean-square error minimization problem using an appropriately regularized Gauss–Newton algorithm. The computation of the Jacobian matrix, a major step in the iteration, is fully described, wherein the forward PDE's and their adjoints are made use of. The experiments, done using composite (poly) vinyl alcohol (PVA) with inhomogeneous stiffness distribution in the central region, are given in Section 5. Reconstruction results are discussed in Section 6 and compared with those from numerically simulated data. Conclusions are put forth in the last section, Section 7.

2. PDE MODEL FOR CORRELATION PROPAGATION

The basic quantity related to the coherence of light, the specific intensity $I(\mathbf{r}, \hat{k}_s, \tau)$ at point $\mathbf{r}$ and time τ in the direction given by the unit vector, $\hat{k}_s$, propagates through a turbid medium obeying the correlation transport equation (CTE) [10]. In a medium where scattering predominates, an angle-averaged version of $I(\mathbf{r}, \hat{k}_s, \tau)$ given by $G(\mathbf{r}, \tau) = \int_{4\pi} I(\mathbf{r}, \hat{k}_s, \tau)\mathrm{d}\hat{k}_s$ and referred to as the amplitude autocorrelation, obeys the following diffusion equation:

$$-\nabla \cdot \kappa \nabla G(\mathbf{r}, \tau) + (\mu_a + 2\mu_s' k_0^2 D_B \tau) G(\mathbf{r}, \tau) = S_0(\mathbf{r} - \mathbf{r}_0). \tag{2.1}$$

Here $\kappa = \frac{1}{3(\mu_a + \mu_s')}$ is the optical diffusion coefficient, and μ_a and μ_s' are the optical absorption and (reduced) scattering coefficients, respectively. Moreover, D_B is the particle diffusion coefficient of the medium, k_0 is the modulus of the light propagation vector, and S_0 is the strength of the isotropic point source at $\mathbf{r}_0$. The term $2\mu_s' k_0^2 D_B \tau$ is owing to the Brownian motion of the scattering centers induced by the background temperature and we denote it by $B(\mathbf{r}, \tau)$. When a focused US beam insonifies the object, it produces in the focal region (the ROI) a refractive index modulation (Δn) and leaves a complex dynamics which looks like noisy aperiodic oscillations in the scattering centers therein. The ROI is approximately hyperboloidal in shape whose volume and length-to-width ratio can be tailored by the parameters such as the focal length f and f/no of the focusing US transducers [11]. Considering the tissue-like medium almost incompressible with a Poisson ratio close to 0.5, we neglect Δn and consider only the dynamics of the scattering centers resulting in a perturbation term in

Eq. (2.1). The result is that $G(\mathbf{r},\tau)$ is perturbed to $G(\mathbf{r},\tau)+G^{\delta}(\mathbf{r},\tau)$ and Eq. (2.1) becomes

$$-\nabla\cdot\kappa\nabla(G+G^{\delta})(\mathbf{r},\tau)+(\mu_a+B(\mathbf{r},\tau)+A(\tau)\chi_I p(\mathbf{r},\tau))(G+G^{\delta})(\mathbf{r},\tau)=S_0(\mathbf{r}-\mathbf{r}_0). \quad (2.2)$$

Here the perturbation term on the left-hand side is denoted by $A(\tau)\chi_I p(\mathbf{r},\tau)$, where $A(\tau)=c\sin^2\frac{\omega_a\tau}{2}$ and χ_I is the characteristic function over I, the insonified ROI. Furthermore, ω_a is the acoustic frequency in radians and c is a constant depending on l^*, the acoustic wave vector k_a, the viscoelastic and the elasto-optic coefficients of the material of the object [12]. We note that the representation of the dynamics by $\sin^2\frac{\omega_a\tau}{2}$ is at best an inadequate approximation. For a correct model one needs to take into account the behavior of scattering centers in a typical viscoelastic medium. A generalized Langevin equation (GLE), which takes into account the history-dependent behavior of the particle wherein the interaction of the particle with the surrounding bath particles is modeled by a multiplicative noise affecting the stiffness constant in the model, is required. This derivation of the appropriate GLE and its solution are beyond the scope of the present work. Details of such a model for a typical scattering particle executing temperature-induced fractional Brownian motion in the presence of an external sinusoidal forcing can be found in [13]. In the absence of such a model, we rely on the sinusoidal approximation of $A(\tau)$ given above. Equation (2.2) is supplemented with the Robin-type boundary condition

$$(G+G^{\delta})(\mathbf{r},\tau)+\kappa\frac{\partial(G+G^{\delta})(\mathbf{r},\tau)}{\partial\mathbf{n}}=0. \quad (2.3)$$

With the material properties of the ROI and the US-induced oscillations as input data, Eqs. (2.2) and (2.3) can be solved to get $(G+G^{\delta})(\mathbf{r},\tau)$ which is the forward solution of the UMOT problem. This facilitates computing M, which is the measurement given by

$$M(p,\mathbf{r},\omega)=\left|\int_0^{\infty}(G+G^{\delta})(\mathbf{r},\tau)e^{-i\omega\tau}\mathrm{d}\tau\right|_{\omega=\omega_a}. \quad (2.4)$$

Yet another related measurement is obtained from $G^{\delta}(\mathbf{r},\tau)$ that is readily computable from the perturbation Eqs. (2.6) and (2.7) (to be given below):

$$M_1(p,\mathbf{r},\omega_a)|_{\mathbf{r}\in\partial\Omega}=\left|\int_0^{\infty}G^{\delta}(\mathbf{r},\tau)e^{-i\omega\tau}\mathrm{d}\tau\right|_{\omega=\omega_a}. \quad (2.5)$$

In an experiment, intensity autocorrelation is measured, from which $M(p,\mathbf{r},\omega)$ is computed; however, M_1 is easily obtained from M by subtracting the background pedestal from M at $\omega=\omega_a$. With this measurement, (a part of) the inverse problem of UMOT is the recovery of $p(\mathbf{r})$ given $M_1(p,\mathbf{r},\omega_a)$, where Eqs. (2.2) and (2.3) represent the forward model of correlation diffusion in a turbid object. In order to facilitate this inversion, we first rewrite the forward equation as

$$-\nabla\cdot\kappa\nabla G^{\delta}(\mathbf{r},\tau)+(\mu_a+B(\mathbf{r},\tau)+A(\tau)\chi_I p(\mathbf{r},\tau))G^{\delta}(\mathbf{r},\tau)=A(\tau)\chi_I p(\mathbf{r},\tau)G(\mathbf{r},\tau), \quad (2.6)$$

with the boundary condition

$$G^{\delta}(\mathbf{r},\tau)+\kappa\frac{\partial G^{\delta}(\mathbf{r},\tau)}{\partial\mathbf{n}}=0,\qquad \mathbf{r}\in\partial\Omega. \quad (2.7)$$

The above equation connects $p(\mathbf{r},\tau)$ nonlinearly to $G^{\delta}(\mathbf{r},\tau)$ because of the presence of a term containing $p(\mathbf{r},\tau)$ on the left-hand side (LHS) of it. If we neglect the term containing the product of $G^{\delta}(\mathbf{r},\tau)$ and $p(\mathbf{r},\tau)$ from the LHS of Eq. (2.6), then it becomes linear in the unknown p rendering the inversion of p using Eqs. (2.6) and (2.7) computationally more expedient. When we use the linearized perturbation equation given by

$$-\nabla\cdot\kappa\nabla G^{\delta}(\mathbf{r},\tau)+(\mu_a+B(\mathbf{r},\tau))G^{\delta}(\mathbf{r},\tau)=A(\tau)\chi_I p(\mathbf{r},\tau)G(\mathbf{r},\tau), \quad (2.8)$$

the following simplifications in the computation accrue [5]. For example, the derivatives once evaluated at the start need not be updated at the end of each iteration, but only measurement error $M-M(\mathbf{p})^i$. Also the PDE part of the Frechet derivative operator retains the structure of the forward propagation PDE [Eq. (2.1)]. Consequently, for the computation of the Jacobian one can use the adjoint of Eq. (2.1). The finite element (FE) discretization of the PDE [Eqs. (2.6) and (2.7)] leads to a set of linear algebraic equations represented by

$$K(p)G^{\delta}=\mathbf{q}, \quad (2.9)$$

where $K(p)$ is the system matrix and $\mathbf{q}$ is the source vector. As indicated earlier, we have used this equation, derived from the linearized version of the perturbation equation [Eq. (2.8)], in our inversion scheme. In accordance with the simplified data collection strategy (i.e., of measuring modulation depth for a set of US frequencies at only one or two detector locations) we sweep the US frequency. When the forcing frequency is changed the amplitude of vibration of the scattering centers change, resulting for each frequency a set of new $p(\mathbf{r})$'s for a given $E(\mathbf{r})$. To compute the data M_1 we use these $p(\mathbf{r})$'s first in Eq. (2.8) and then in Eq. (2.5).

3. MOMENTUM BALANCE EQUATION

Here, the object under consideration is only the ROI, Ω_f, the portion insonified by the focusing US transducer where the displacement is nonzero. In contrast, the focal region is defined to be the support of the US transducer-induced radiation force. To find Ω_f, we first compute the US force [14] corresponding to an approximated focal region (e.g., by incorporating the nodes where the force exceeds a small fraction of its maximum in a central node) and then solve for displacement via the momentum balance equation for the entire object, now considered an infinite medium vis-à-vis the focal region. The internal Dirichlet boundary $\partial\Omega_f$ thus separates the zero-displacement region of the object from the rest.

Toward computing the displacement field via an inversion of the momentum balance equation, a plane stress approach based on a 2D linear elasticity setup is adopted, with the ROI material being assumed to be nearly incompressible. Under strictly sinusoidal US forcing and the linear elasticity framework, the vibrating ROI would exhibit sinusoidal response with the frequency of the excitation once the transients die out. Accordingly, the so-called mixed form of the governing equations [in terms of the amplitude $u_0(\mathbf{r})$ of the displacement

vector field $u(\mathbf{r}, t) = (\mathbf{u}(\mathbf{r}, t), q(\mathbf{r}, t))^T$ and the pressure field $q(\mathbf{r})$] takes the form [15]

$$\rho\omega^2 u_0 + \nabla \cdot \left(-qI + \frac{E}{2(1+\nu)}(\nabla u_0 + (\nabla u_0)^T)\right) = f_0; \quad \mathbf{r} \in \Omega_f, \tag{3.1a}$$

$$\nabla \cdot u_0 = \frac{q(1+\nu)(1-2\nu)}{E\nu}; \qquad \mathbf{r} \in \Omega_f, \tag{3.1b}$$

$$u_0 = 0 \qquad \text{for } \mathbf{r} \in \partial\Omega_f. \tag{3.1c}$$

Here E denotes Young's modulus, ν Poissons ratio, ρ the material density, $f_0(\mathbf{r})$ the forcing amplitude, and q the pressure, all referred to the undeformed configuration. Finally, ω denotes the US forcing frequency. Within the FE method, Eq. (3.1) may be successfully solved via a mixed weak formulation even as the material approaches the incompressibility limit, i.e., as ν approaches 0.5. The problem involved in the weak formulation is to find $u = (u_0, q) \in H^1(\Omega_f) \times L^2(\Omega_f)/\mathbb{R}$ so as to satisfy

$$B(w, u) = (\mathrm{w}, \mathrm{f}_0), \quad \forall\ w = (\mathrm{w}, \varphi) \in H_0^1(\Omega_f) \times L^2(\Omega_f). \tag{3.2}$$

Here $(\mathrm{w}, \mathrm{f}_0) = \int_{\Omega_f} \mathrm{w} \cdot \mathrm{f}_0 \mathrm{d}\Omega_f$ is the linear form and $B(w, u)$ the bilinear form defined as

$$B(w,u) = \int_{\Omega_f} \left(\rho\omega^2 w \cdot u_0 - [\nabla w + \nabla w^T] : \left[\frac{E}{4(1+\nu)}(\nabla u_0 + (\nabla u_0)^T)\right]\right)\mathrm{d}\Omega_f + \int_{\Omega_f}\left((\nabla \cdot w)q + \varphi \nabla \cdot u_0 + \frac{\varphi q}{\beta E}\right)\mathrm{d}\Omega_f, \tag{3.3}$$

where β is a large scalar multiplier ensuring that the bulk modulus is much higher than E. Indeed, the pressure q can be eliminated using Eq. (3.1b) and one can get a weak formulation for u_0 alone. In the FE implementation, Eq. (3.2) may finally be reduced to the matrix-vector equation given by

$$K^h u^h = s^h, \tag{3.4}$$

where h denotes the characteristic element size, K^h the so-called stiffness matrix, u^h the unknown vector (in general consisting of both the nodal displacement amplitudes and pressure), and s^h the source vector. Equation (3.4) is inverted for u^h and $p(\mathbf{r}) \cong \langle |u^h(\mathbf{r})|^2 \rangle$.

4. DIRECT RECOVERY OF YOUNG'S MODULUS FROM MODULATION DEPTH

We introduce the operator $F_1(\mu_a, p, \kappa) = G_\delta$ through Eq. (2.8) and the measurement operator $M_1(G_\delta) = M_1$ through Eq. (2.5). Then the composite operator $F_A = M_1 \circ F_1$ maps p to M_1. Similarly, we introduce $F_2(E, \rho, \nu) = u$ using Eq. (3.1), the measurement operator $M_2(u) = p$ through $p(\mathbf{r}) = \langle |u(\mathbf{r})|^2 \rangle$, and the composite operator $F_B = M_2 \circ F_2$ which maps E to $p(\mathbf{r})$. With these, we define the operator $F = F_A \circ F_B$ which maps E to M_1, the measurement from the UMOT experiment. Our attempt is to recover E from M_1 through the (direct) inversion of F.

We invert the equation $F = M_1(E)$ for E by solving the following nonlinear minimization problem:

$$\underset{E \in L^\infty(\Omega_f)}{\text{minimize}}\, \Theta(E) = \frac{1}{2}\|F(E) - M_1\|^2_{L^2(\partial\Omega_f)} + \frac{\lambda}{2}\|E\|^2_{L^2(\Omega_f)}. \tag{4.1}$$

Here λ is an appropriate regularization parameter. We employ the Gauss–Newton algorithm to accomplish this minimization through the iteration

$$E^{i+1} = E^i - (H(E^i))^{-1} G(E^i), \tag{4.2}$$

where H and G are the Hessian and gradient, respectively, of the error functional Θ evaluated at E^i using

$$H(E)\delta E = (DF^*(E)DF(E) + \lambda I)\delta E \tag{4.3a}$$

and

$$G(E) = DF^*(F(E) - M_1). \tag{4.3b}$$

Here I denotes the identity matrix, δE is an increment in E, and DF and DF^* are, respectively, the Frechet derivative and its adjoint of F. The Frechet derivative, or more appropriately its finite dimensional equivalent, the Jacobian, is a matrix whose elements are the rate of change of measurement(s) with respect to nodal values of E. This is obtained by combining the derivatives of M_1 with respect to $\mathbf{p}$ [which is the discretized version of $p(\mathbf{r})$] and those of E with respect to $\mathbf{p}$.

From the CDE we have derivatives of the type $\frac{\partial M_{1i}}{\partial p_j}$, the computation of which should involve two forward solves of the CDE. A complete row of the Jacobian matrix can be computed with only one forward solve of the CDE and its adjoint, making use of the reciprocity relation which light diffusion obeys [5]. Similarly, for $\frac{\partial p_i}{\partial E_j}$, the momentum balance equation [Eq. (2.3)] and its adjoint as given in [15] can be made use of. However, since the number of unknowns in Ω_f and the number of measurements are equal, the computational advantage of using the adjoint formulation, in this case, is little; therefore, for this part, we use the perturbation scheme which involves two forward solves for each nodal unknown.

In order to compute a typical element of the Jacobian matrix $J = \{\frac{\partial M_{1i}}{\partial E_j}\}$ one should consider the fact that a change in E at a typical node, δE_j, necessarily results in changes of $\mathbf{p}$ at all nodes. Therefore, $(\partial M_{1i}/\partial E_j) = \sum_{k=1}^{k=N} (\partial M_{1i}/\partial p_k)(\partial p_k/\partial E_j)$; the evaluation of this requires all the N derivatives of the type $\frac{\partial p_k}{\partial E_j}$, where N is the number of nodes. The set of all derivatives is evaluated using the appropriate forward Eqs. (2.6), (2.7), and (3.1).

Once the derivatives are computed, Eq. (4.3) is set up and the ith increment, δE^i, is obtained from it. A direct inversion of $H(E^i)$ is not attempted; instead a second optimization step using a conjugate gradient search to reach the optimal point is employed. The algorithm is stopped when the norm of

the error between the experimental measurement and its computed counterpart falls below a preset small value.

5. EXPERIMENTS USING PVA PHANTOMS

A. Details of Phantom Fabrication

The PVA phantoms are fabricated using the method described in [16,17]. We rely on only the air bubbles trapped during the cooling–thawing cycles to give the phantom a tissue-like scattering coefficient (μ_s) and do not introduce additional scattering centers. Therefore, the (μ_s') (reduced scattering coefficient) obtained is only approximately 8.0 cm^{-1} and not high enough to mimic human tissue. Similarly, an external absorber like India ink was not added, with the result that the absorption coefficient (μ_a) is uniform at a low value 0.1 cm^{-1}. The mechanical properties of the fabricated samples are density (ρ) = 1000 Kgm^{-3}, $\nu = 0.49$, $E = 11.3$, and 22.39 kPa. The objects were fabricated as slabs of dimension 3.5 cm × 3.5 cm × 3.5 cm. The two composite slabs are made by sandwiching first a thin slice (thickness 0.5 cm) of 22.39 kPa material in between two slabs of background Young's modulus of 11.3 kPa and then two slices of 22.39 kPa (thickness 0.5 cm) at the ends of a single slab of background Young's modulus of 11.3 kPa, to make the composite of thickness 3.5 cm.

B. Experimental Setup and Data Collection

The schematic diagram of the experimental setup is given in Fig. 1. The PVA phantom is insonified by a two-region confocal US transducer. The two regions are driven by power amplifiers that take inputs from the same ultrastable, dual channel function generator, at frequencies of 1 MHz and 1 MHz + Δf Hz. The difference Δf can be varied from a few tens of Hz to 1–2 kHz. At the common focal region, the ROI, the two acoustic waves interfere producing also a force field, at the difference frequency, which is assumed to be almost sinusoidal. An unexpanded laser beam (from a He–Ne laser of 15 mW, Thorlabs) is introduced from one side of the slab. On the diametrically opposite side, a single-mode fiber is carefully aligned to capture one laser speckle to maximize the signal-to-noise ratio of the detected modulated intensity. The focal region of the US transducer is approximately hyperboloidal in shape of length and width of the waist region ≈1.42 cm and 0.2 cm, respectively. For acoustic impedance matching, both the transducer and the composite slab are immersed in water. The transducer itself is mounted on a rotation-cum-translation stage and aligned such that the ROI intercepts the region where the inhomogeneity is [see Figs. 1(a) and 1(b)]. In the first experiment, as shown in Fig. 1(a), the US transducer is aligned so that the laser beam passes through a central hole in the transducer and diffuses along its axis. The modulated intensity, as captured by the single-mode fiber from a single speckle is given to a photon-counting photo-multiplier tube (PMT), Hamamatsu H7360-03. The current from the PMT is given to a signal conditioner and converted into voltage and given to a hardwired autocorrelator. From the autocorrelator we get intensity autocorrelation, $g_2(\tau) = \int_0^\infty I(t)I(t+\tau)dt \equiv \langle I(t)I(t+\tau)\rangle$. From $g_2(\tau)$, $g_1(\tau)$ is computed using the Seigert relation [6]. [The hardwired autocorrelator is a digital device which samples the incoming signal and computes $g_2(\tau)$ for a specified duration. Here we have set this duration as 15–20 min. We can also set the sampling time depending upon the maximum frequency of the signal of our interest. We have chosen 100 μs as the sampling time. The finite memory in the autocorrelator and the selected sampling time put a limit on the number of samples of $g_2(\tau)$ one can gather. In our case, this number (L) was kept at 2048.]

The data, which is the modulation depth in $g_1(\tau)$ (M) is obtained as the modulus of the Fourier transform of $g_1(\tau)$ evaluated at Δf Hz. From M, the data M_1 is computed as described in Section 2. As stated earlier, we enrich the data set by varying Δf. The collected set of M_1 as Δf is swept from 200 to 700 Hz is shown in Figs. 2 and 3. The variation of M_1 is considerable in the range of Δf used in the experiment; in fact, M_1 goes through resonance-like peaks in this range (for example, Fig. 3).

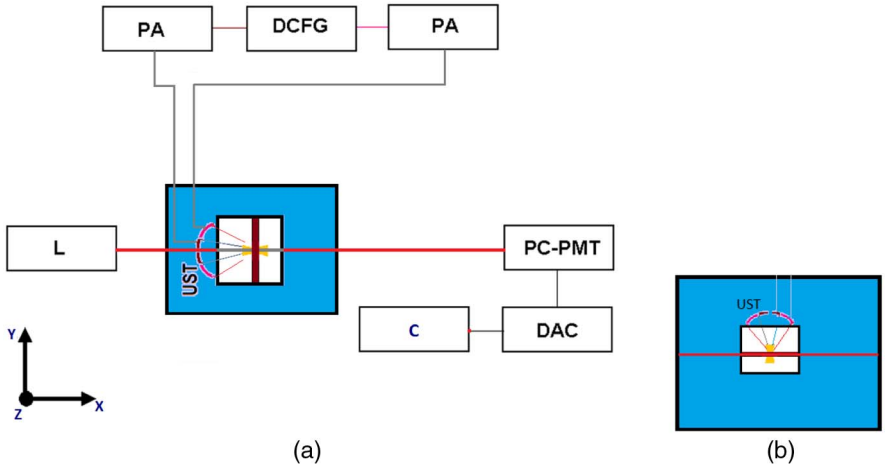

Fig. 1. Unexpanded beam from the laser source L illuminates the ROI insonified by a confocal ultrasound transducer (UST). The scattered intensity of the light is detected by the photo-multiplier tube (PC-PMT) and given to the correlator DAC and then to a computer C. The UST is driven by power amplifiers (PA) that take input from a dual-channel function generator (DCFG).

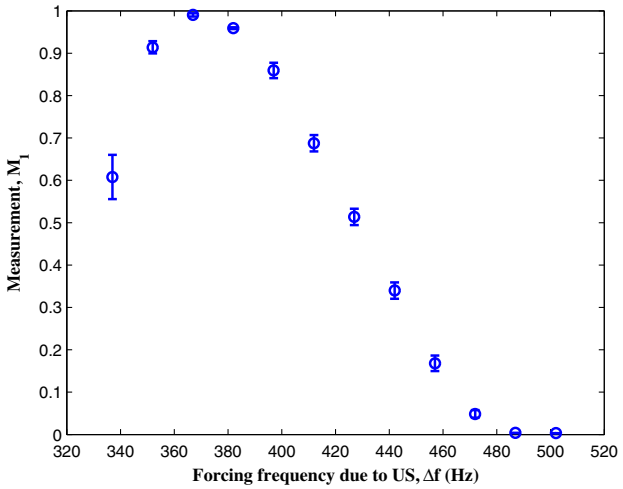

Fig. 2. Experimental measurements (M_1) corresponding to object 1 with illumination as in Fig. 1(a).

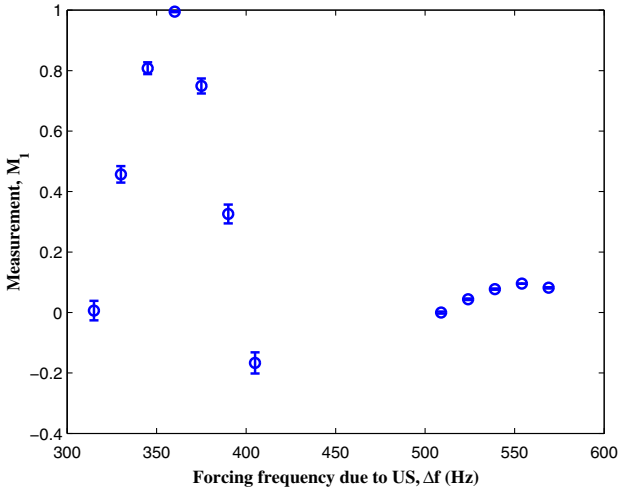

Fig. 3. Experimental measurements (M_1) corresponding to object 2 with illumination as in Fig. 1(a).

Since, from our experience, data from a single source position is found to be not quite adequate for a proper recovery of E, we have also collected data from a second detector position [see Fig. 1(b)]. Since the alignment of the single-mode fiber is very cumbersome, it was decided to rotate the US transducer by 90° and acquire a new set of data. These experiments are repeated with both the composite phantoms, fabricated as described in Section 5.A. Data collected with this arrangement are shown in Figs. 4 and 5.

The hyperboloidal shape of the focal region of the US transducer is verified through solving the Westervelt equation [14] dealing with high-intensity acoustic wave propagation. The pressure gives rise to acoustic radiation force in the focal region, which is computed and shown in Fig. 6.

In addition to the experimental data, we have also collected data from numerical simulations. We have employed the same

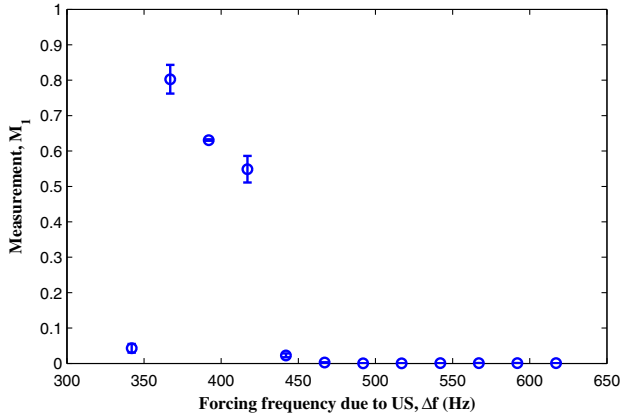

Fig. 4. Experimental measurements (M_1) corresponding to object 1 with illumination as in Fig. 1(b).

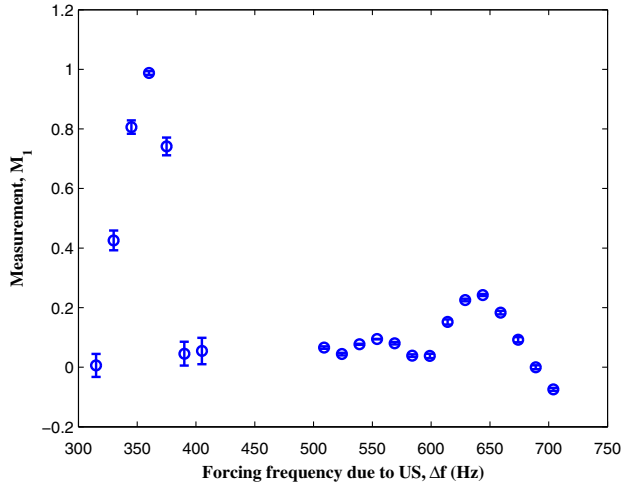

Fig. 5. Experimental measurements (M_1) corresponding to object 2 with illumination as in Fig. 1(b).

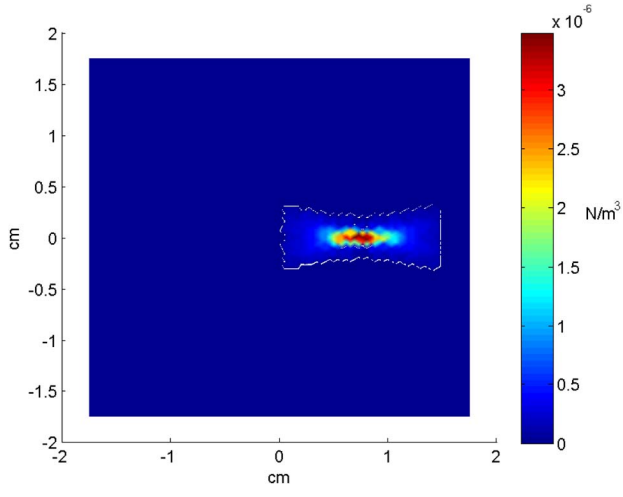

Fig. 6. Computed ultrasound force density distribution. It is seen that the focal region is approximately hyperboloidal.

geometry and objects (same shape, size, and optical as well as mechanical properties) as used in the experiments, in the numerical simulations. Keeping up with the experiments, data were collected only at two detectors kept 90° apart. For this, we have solved the CDE, Eq. (2.8) and its discretized version Eq. (2.9) as well as the momentum balance equation [Eq. (3.1) and its discretized version Eq. (3.4)].

In all the numerical algorithms, both for generating data and for inverting the numerically simulated and experimentally generated data using the Gauss–Newton algorithm, we have used 2D objects which are cross sections of the hyperboloidal ROI containing the US transducer axis. We note that a plane stress approximation is not necessarily valid for any cross section of the ROI. However, to demonstrate the recovery of both the location and quantitative variation therein of the inhomogeneities in E in a computationally expedient manner, we chose to restrict ourselves to tackling the inverse problem corresponding to the recovery of 2D objects in the present work. The rectangular object region of dimension 3.5 cm × 3.5 cm is discretized using an FE mesh with 13,168 triangular elements and 6740 nodes. For this object with the mechanical and optical properties specified, the measurement is computed by solving the two forward equations. By varying the beat frequency, Δf, (in our case from 300 to 700 Hz) we have generated a set of M_1 using the two detectors. The numerical data is obtained from M_1 by adding 1%–4% noise to it.

The data generated, both through numerical simulations and experiments, are input to the Gauss–Newton algorithm as developed in Section 4 to recover E. The updates for E are obtained by inverting the perturbation equation [Eq. (4.3)], one of the important steps in the inversion algorithm. Equation (4.3) is solved for δE using the conjugate gradient search scheme. The perturbation equation itself is updated at the end of each iteration through recomputing the Jacobian and the computed M_1 corresponding to the $E(\mathbf{r})$. A regularization term, λI (here λ is the regularization parameter and I is the identity matrix) is formally employed in Eq. (4.3), wherein λ is taken negligibly small, i.e., 3.2116×10^{-54} at the start of the inner iteration, and reduced by a factor of 1.5 at each iteration.

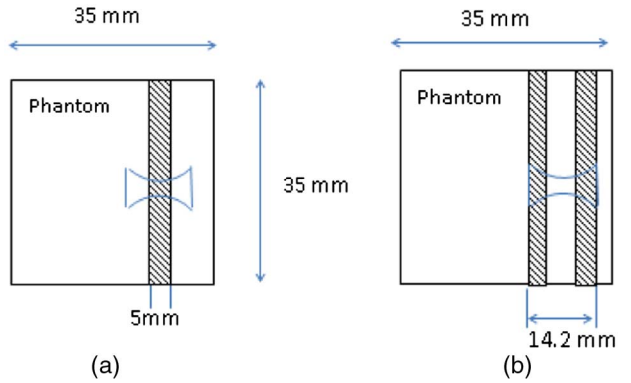

Fig. 7. Cross section of the composite PVA phantom showing the inhomogeneity and the ultrasound focal region. The hatched region has storage modulus 22.39 kPa and the other 11.3 kPa. (a) Object 1 and (b) object 2.

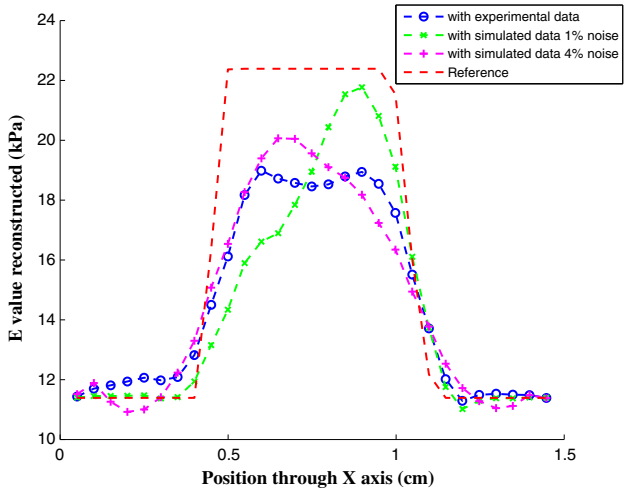

Fig. 8. Cross section through the center of the reconstruction shown in Fig. 10 compared with that of original shown in Fig. 12.

6. RESULTS AND DISCUSSION

The results of iterative recovery are presented in two separate sets of figures which correspond to the two different inhomogeneity distributions shown in Fig. 7. The cross sections, through the center of the inhomogeneity, of the reconstructions obtained from simulated data are shown in Figs. 8 and 9 when the noise in data is increased from 1% to 4%. In all the cases the algorithm converged in 6–10 iterations when the mean-squared error in the measurement space $[\varepsilon(n) = \|M_1^{\epsilon} - M_1^{C_n}\|^2$, where M_1^{ϵ} is the experimental measurement and $M_1^{C_n}$ is its computed counterpart at the nth iteration] decreased to 1.2935×10^{-17} for case (a) and to 6.5435×10^{-18} for case (b). From this exercise we see that the reconstruction algorithm has a robust behavior against data noise and the contrast recovery in the inhomogeneous inclusion is reasonably good.

The experimental data from the two views of Fig. 1 (altogether 126 measurements with 63 from each view) are also input to the Gauss–Newton algorithm. Reconstructions, gray-scale images, for the two objects are shown in Figs. 10 and 11 (original gray-scale images in Figs. 12 and 13). The corresponding cross-sectional plots through the center of the inhomogeneous inclusion are in Figs. 8 and 9. The data domain mean-square error plots with iteration number, for the two objects considered, are shown in Figs. 14 and 15. It is seen that the error reduced to 2.0×10^{-24} (in 11 iterations) for object (a) and to 3.0×10^{-23} (in 6 iterations) for object (b). The cross-sectional plots are a pointer to the faithfulness of recovery of E. We have thus proven that by scanning the US frequency it is possible to generate linearly independent data sets for UMOT which goes a long way in making the experimental data collection less tedious; and they are good enough for a

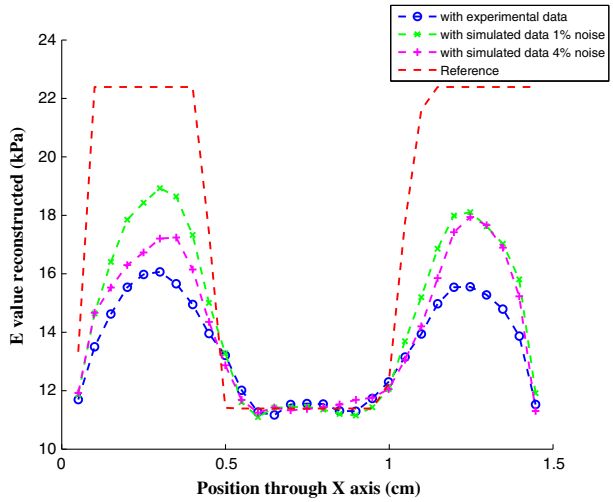

Fig. 9. Same as that of Fig. 8 corresponding to the reconstruction shown in Fig. 11.

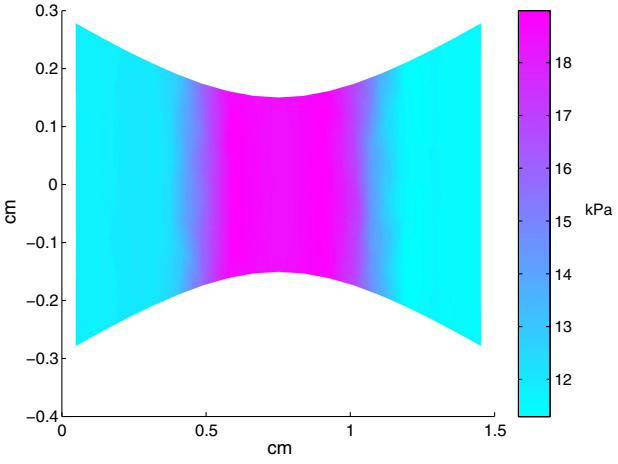

Fig. 10. Reconstruction in the ROI for object 1 corresponding to the inhomogeneity distribution shown in Fig. 12.

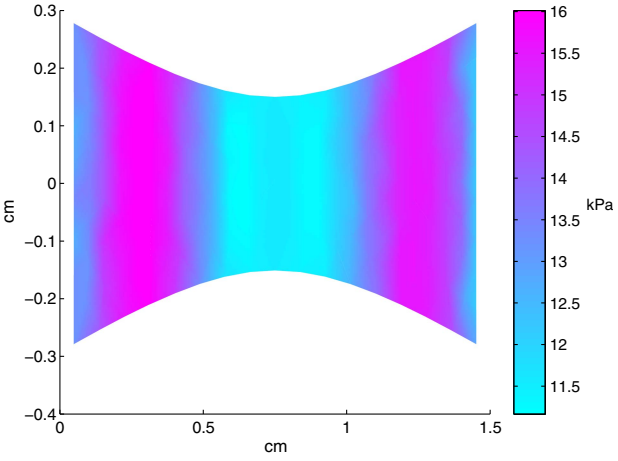

Fig. 11. Reconstruction in the ROI for object 2 corresponding to the inhomogeneity distribution shown in Fig. 13.

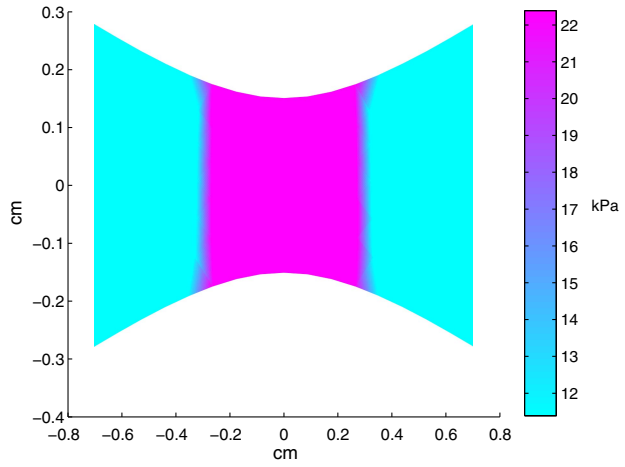

Fig. 12. Elasticity distribution of object 1 [Fig. 2(a)] in the focal region of the US transducer.

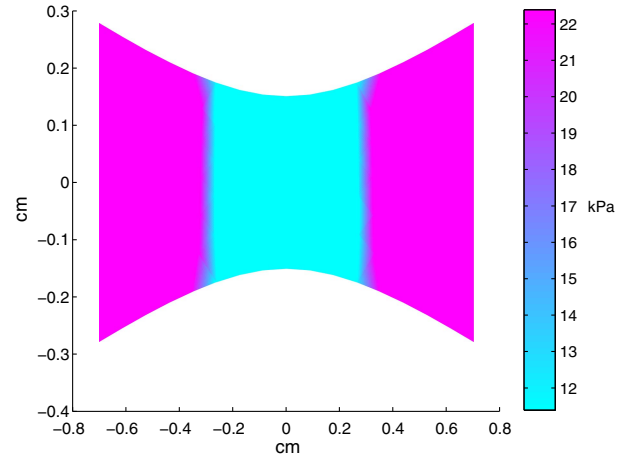

Fig. 13. Same as Fig. 12 but for object 2 shown in Fig. 7(b).

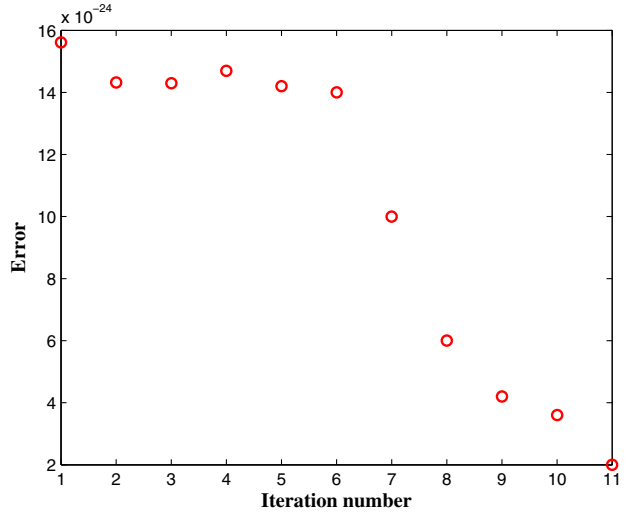

Fig. 14. Data domain mean-square error versus iteration number whilst reconstructing object 2.

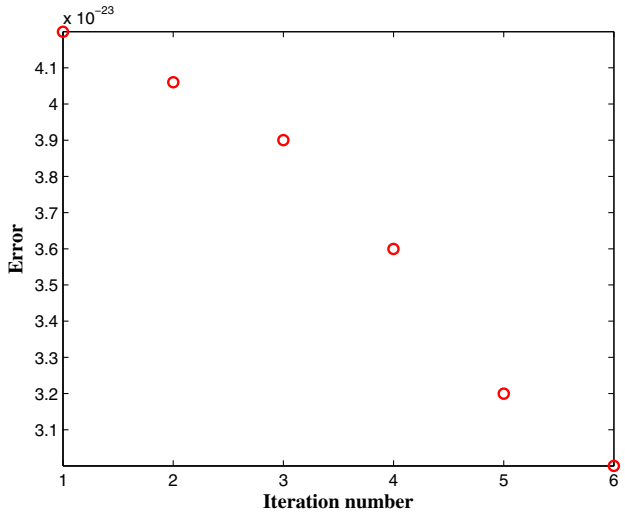

Fig. 15. Data domain mean-square error versus iteration number whilst reconstructing object 1.

reasonably accurate, spatially resolved tomographic recovery of $E(\mathbf{r})$ in the US focal region.

7. CONCLUSIONS

We have devised a new scheme to recover Young's modulus distribution from experimental UMOT data, gathered only at two detector locations but at many acoustic frequencies. When the US frequency varies, so does the amplitude of mechanical oscillations the US force produces in the scattering centers. Therefore, if one retains $p(\mathbf{r})$ as the set of unknowns, which is related to the above amplitude, the reconstruction problem becomes too ill-conditioned to be amenable to any meaningful solution. We, in this work, prevented this blow-off of the set of unknowns by projecting $p(\mathbf{r})$ via the momentum balance equation to the material property $E(\mathbf{r})$, which remains invariant to the US frequency sweep. This along with the consequent simplification achieved in the experimental data collection are the new contributions of the present work. With reconstructions from numerical data, it is shown that, within reasonable limits, the algorithm is insensitive to variations in noise levels in the data.

The Gauss–Newton algorithm is dependent on the sensitivity of the data-to-material property distribution. Because light travels through a multitude of paths owing to diffusion, this sensitivity can be greatly compromised when dealing with interior nodes far removed from the boundary. Here, one of our recently developed algorithms using a stochastic search scheme which does not explicitly use a derivative, has been shown to be of great use to recover the unknowns belonging to such interior nodes, in the context of photoacoustic tomography [18]. Replacement of the Gauss–Newton scheme with such a stochastic optimization scheme, it is hoped, might improve the reconstruction in the present case as well.

REFERENCES

1. L. H. V. Wang, S. L. Jacques, and X. M. Zhao, "Continuous wave ultrasonic modulation of scattered laser light to image objects in turbid media," Opt. Lett. **20**, 629–631 (1995).
2. M. Kempe, M. Larionov, D. Zaslavsky, and A. Z. Genack, "Acousto-optic tomography with multiply scattered light," J. Opt. Soc. Am. A **14**, 1151–1158 (1997).
3. L. V. Wang, "Mechanisms of ultrasonic modulation of multiply scattered coherent light: an analytic model," Phys. Rev. Lett. **87**, 043903 (2001).
4. G. Yao and L. V. Wang, "Theoretical and experimental studies of ultrasound-modulated optical tomography in biological tissue," Appl. Opt. **39**, 659–664 (2000).
5. H. M. Varma, K. P. Mohanan, N. Hyvonen, A. K. Nandakumaran, and R. M. Vasu, "Ultrasound-modulated optical tomography: recovery of amplitude of vibration in the insonified region from boundary measurement of light correlation," J. Opt. Soc. Am. A **28**, 2322–2331 (2011).
6. B. J. Berne and R. Pecora, *Dynamic Light Scattering* (Dover, 2000).
7. A. Li, Q. Zhang, J. P. Culver, E. L. Miller, and D. A. Boas, "Reconstructing chromophore concentration images directly by continuous-wave diffuse optical tomography," Opt. Lett. **29**, 256–258 (2004).
8. H. K. Kim, M. Flexman, D. J. Yamashiro, J. J. Kandel, and A. H. Heilscher, "PDE-constrained multispectral imaging of tissue chromophores with the equation of radiative transfer," Biomed. Opt. Express **1**, 812–824 (2010).
9. R. Sriram Chandran, D. Roy, R. Kanhirodan, R. M. Vasu, and C. Usha Devi, "Ultrasound modulated optical tomography: Young's modulus of the insonified region from measurement of natural frequency of vibration," Opt. Express **19**, 22837–22850 (2011).
10. S. Sakadzic and L. V. Wang, "Correlation transfer and diffusion of ultrasound-modulated multiply scattered light," Phys. Rev. Lett. **96**, 163902 (2006).
11. E. Konofagou, J. Thierman, and K. Hynynen, "A focused ultrasound method for simulation, diagnostic and therapeutic applications: a simulation study," Phys. Med. Biol. **46**, 2967–2984 (2001).
12. S. Sakadzic and L. V. Wang, "Ultrasonic modulation of multiply scattered coherent light: an analytical model for anisotropically scattering media," Phys. Rev. E **66**, 026603 (2002).
13. S. Sarkar, S. Roy Chowdhury, D. Roy, and R. M. Vasu, "Internal noise driven generalized Langevin equation for modelling non-local continnum," Phys. Rev. E (under review).
14. T. Kamakura, T. Ishiwata, and K. Matsuda, "Model equation for strongly focused finite-amplitude sound beams," J. Opt. Soc. Am. A **18**, 3035–3046 (2001).
15. A. A. Oberai, N. H. Gokhale, and G. R. Feijoo, "Solution of inverse problems in elasticity imaging using the adjoint method," Inverse Probl. **19**, 297–313 (2003).
16. C. Usha Devi, R. M. Vasu, and A. K. Sood, "Design, fabrication and characterization of tissue-equivalent phantoms for optical elastography," J. Biomed. Opt. **10**, 0440201 (2005).
17. C. U. Devi, R. M. Vasu, and A. K. Sood, "Application of ultrasound-tagged photons for measurement of amplitude of vibration of tissue caused by ultrasound: theory, simulation, and experiments," J. Biomed. Opt. **11**, 049802 (2006).
18. S. Sarkar, D. Roy, and R. M. Vasu, "A perturbed martingale approach to global optimization," Phys. Lett. A **378**, 2831–2844 (2014).